Available online at www.sciencedirect.com
SCIENCE DIRECT®
Journal of Computational Physics 191 (2003) 228–248
JOURNAL OF COMPUTATIONAL PHYSICS
www.elsevier.com/locate/jcp

Numerical simulation of the plasma of an electron cyclotron resonance ion source

Alain Girard [a,*], Christian Lécot [b], Konstantin Serebrennikov [a]

[a] *Département de Recherche Fondamentale sur la Matière Condensée, SBT, CEA Grenoble, 17 rue des Martyrs, 38054 Grenoble Cedex 9, France*
[b] *Laboratoire de Mathématiques, Université de Savoie, Campus scientifique, 73376 Le Bourget-du-Lac Cedex, France*

Received 20 December 2002; received in revised form 4 June 2003; accepted 5 June 2003

Abstract

We propose a kinetic description of the particles in an electron cyclotron resonance ion source (ECRIS) for highly charged ion production. The electron distribution function (EDF) is solution of a Fokker–Planck equation in velocity space. A new finite-volume scheme for the computation of the EDF is presented. The system is azimuthally symmetric. A two-dimensional, structured grid of quadrangles is used to describe the geometry in spherical polar coordinates (v, μ). The temporal stiffness problems are addressed with a semi-implicit method of time integration. Evaluation of the coefficients of the collision operator requires derivatives of the Rosenbluth potentials in every time step. The computation is accomplished through parallel implementation. Examples of the application of the algorithm are given and the role of the different design parameters is studied.

AMS: 65M60; 82D10

Keywords: Electron cyclotron resonance ion source; Finite volume method; Fokker–Planck equation; Electron distribution function; Radio-frequency heating

1. Introduction

An ECRIS is a mirror machine for producing multicharged ion beams [1,2]. Fig. 1 shows a schematic drawing of an ECRIS. It is an open-ended magnetic trap that confines a hot electron plama. Two coils (1) and (2) produce a mirror field and a multipole (3) generates a radial field. The resulting field leads to a minimum-B structure. A radio-frequency (RF) wave is injected into the plasma to heat the electrons. The magnetic configuration leads to a closed resonance surface (4).

* Corresponding author. Tel.: +33-4-3878-4365; fax: +33-4-3878-5160.
E-mail addresses: agirard@cea.fr (A. Girard), Christian.Lecot@univ-savoie.fr (C. Lécot).

0021-9991/$ - see front matter © 2003 Elsevier B.V. All rights reserved.
doi:10.1016/S0021-9991(03)00312-7

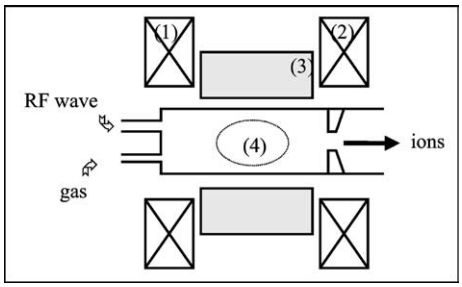

Fig. 1. Electron cyclotron resonance ion source.

The electrons are trapped in the plasma chamber by the mirror effect. The mirror ratio R_m is defined as $R_m = B_{max}/B_{min}$, where B_{max} and B_{min} are the maximum and minimum magnetic inductions, respectively. Electrons whose velocity is mainly parallel to the magnetic field are not confined. The loss region is defined as the region where electrons are not confined. We employ a spherical coordinate system in velocity space,

$$\boldsymbol{v} = \left(v\sqrt{1-\mu^2}\cos\varphi, v\sqrt{1-\mu^2}\sin\varphi, v\mu\right), \tag{1}$$

where $\mu = \cos\theta$ and $\theta = 0$ corresponds to the direction of the axial magnetic field (z axis). The system is then azimuthally symmetric and has a reflection symmetry about the midplane $\mu = 0$. Following [3], the loss angle is given by $\sin^2\theta_{LC} = 1/R_m$. Since the scattering rate of electrons is greater than that of ions, more electrons than ions will tend to leak out of the ends of the device. An ambipolar potential will build up, being greatest at the center and decreasing towards the ends. If Φ is the electrostatic potential, the electron loss region is defined by

$$\sin^2\theta \leqslant \frac{1}{R_m}\left(1 - \frac{v_{pe}^2}{v^2}\right). \tag{2}$$

Here $v_{pe}^2 = (2e/m_e)\Phi$, m_e is the electronic mass and e is the electronic charge. The electron loss region is shown in Fig. 2. We denote by f_e the EDF. If we assume that electrons in the loss region are lost immediately then we set $f_e = 0$ on the loss region boundary.

The losses of electrons are due primarily to the scattering of particles by classical Coulomb collisions into loss regions. The description of this process is given by the Fokker–Planck equations as derived in the paper of Rosenbluth et al. [4] and in the review article of Trubnikov [5]. It is experimentally verified that the density of the plasma is higher in the neighbourhood of the center of the chamber. In our model we assume that the collision process is spatially homogeneous, which leads to a slight overestimate of the collisional rate. The time rate of change of the distribution function $f_a(\boldsymbol{v}, t)$ for particles of species a is given by

$$\left(\frac{\partial f_a}{\partial t}\right)_{coll} = \sum_b L^{a/b}\frac{m_a}{m_b}\frac{\partial}{\partial v_i}\left(f_a\frac{\partial\varphi_b}{\partial v_i}\right) - \sum_b L^{a/b}\frac{\partial}{\partial v_i}\left(\frac{\partial f_a}{\partial v_j}\frac{\partial^2\psi_b}{\partial v_i\partial v_j}\right), \tag{3}$$

where the sum is over all the species of particles (electrons and ions). As usual the summation on repeated indices is understood. Here

$$L^{a/b} = \left(\frac{4\pi e_a e_b}{m_a}\right)^2\lambda,$$

where λ is the Coulomb logarithm. In the present work we use the *Rosenbluth potentials*

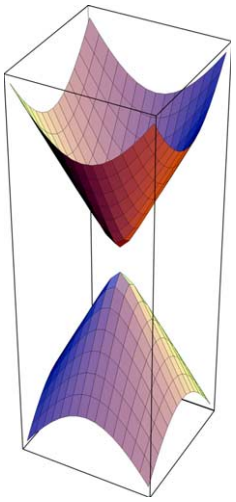

Fig. 2. Electron loss region boundary.

$$\varphi_b(\boldsymbol{v},t) = -\frac{1}{4\pi}\int_{\boldsymbol{R}^3}\frac{f_b(\boldsymbol{v}',t)}{|\boldsymbol{v}-\boldsymbol{v}'|}\,\mathrm{d}\boldsymbol{v}', \quad \psi_b(\boldsymbol{v},t) = -\frac{1}{8\pi}\int_{\boldsymbol{R}^3}|\boldsymbol{v}-\boldsymbol{v}'|f_b(\boldsymbol{v}',t)\,\mathrm{d}\boldsymbol{v}',$$

which were introduced by Trubnikov. These individual functions which refer to particles of one kind b are more convenient than the potential functions g_a and h_a given by Rosenbluth et al. The functions h_a and g_a can be expressed in terms of φ_b and ψ_b by means of the relations

$$h_a = -4\pi\sum_b \frac{m_a+m_b}{m_b}\left(\frac{Z_b}{Z_a}\right)^2\varphi_b, \quad g_a = -8\pi\sum_b\left(\frac{Z_b}{Z_a}\right)^2\psi_b. \tag{4}$$

The RF wave is injected into the plasma and heats the electrons. By bounce averaging, this change of energy can be described as a diffusion process in velocity space: the heating term is derived in the form

$$\left(\frac{\partial f_\mathrm{e}}{\partial t}\right)_{\mathrm{RF}} = \frac{\partial}{\partial v_i}\left(D_{i,j}\frac{\partial f_\mathrm{e}}{\partial v_j}\right), \tag{5}$$

where $\boldsymbol{D}$ is a diffusion tensor (see below).

The full equation for the EDF f_e is then

$$\frac{\partial f_\mathrm{e}}{\partial t} = \left(\frac{\partial f_\mathrm{e}}{\partial t}\right)_{\mathrm{coll}} + \left(\frac{\partial f_\mathrm{e}}{\partial t}\right)_{\mathrm{RF}} + S_\mathrm{i} + S_\mathrm{e}, \tag{6}$$

where the source term S_i is related to the ionization cross section of the gas. An additional source term S_e is included in order to describe electron injection through secondary emission on the walls. Since the ions are cold and collisional, the ionic population is assumed to be Maxwellian.

In a previous article [6] a one-dimensional numerical model was used. The domain in spherical polar coordinates (v,μ) was discretized as the union of rectangular subdomains. In each subdomain the Rosenbluth potentials were assumed to be isotropic. In addition the heating diffusion tensor was reduced to a diagonal tensor. With these assumptions Eq. (6) is separable. In each subdomain, the EDF was represented by its lowest angular eigenfunction and a finite-difference method was used for discretizing the variable v. The time was discretized by a semi-implicit scheme, i.e., the scheme was implicit but the Rosenbluth po-

tentials were treated explicitly. The results showed a good qualitative variation of the EDF with the various parameters [7]. However, there was some quantitative differences between the experimental and the computed values and it was decided to develop a two-dimensional code. In particular the 1D code overestimates the mean electron energy since all the electrons are assumed to interact with the wave in this model.

Fokker–Planck codes were developed at Livermore by Killeen et al. [8–11] for both mirror and toroidal plasmas. The Livermore code was then modified by Karney [12]. The standard two-dimensional Fokker–Planck code of Killeen et al. used finite-differences in (v, θ) space. The Rosenbluth potentials were represented by expansions in Legendre polynomials $P_j(\mu)$. In the computations a finite number of terms in the Legendre expansions were taken. The equations were time-integrated using either alternating-direction (ADI) method, or fully implicit differencing. The Rosenbluth potentials were treated explicitely. When using ADI, several tridiagonal linear systems were obtained. With fully implicit differencing one obtained a system with a nine-banded matrix. Karney only considered a linearized collision operator and used the finite difference method for discretizing the derivatives with respect to v and θ. The method for advancing the Fokker–Planck equation in time was the ADI method. An ionic Fokker–Planck code is described in [13]. The calculation of the Rosenbluth potentials involves solving the Poisson equations

$$\Delta\varphi_e = f_e \quad \text{and} \quad \Delta\psi_e = \varphi_e. \tag{7}$$

The author uses an uniform grid in the rectangular velocity space. The mass-conserving property of the Fokker–Planck operator is taken into account in the numerical algorithm by using a conservative finite difference scheme. Time is discretized by an ADI algorithm.

On the other hand, great efforts were made to construct conservative and entropy decaying schemes for the Fokker–Planck equation. Such schemes aim to satisfy discrete analogues of the properties of the continuous equation: these are conservation of mass, momentum and energy, the characterization of the equilibrium states by Maxwellians and the decay of entropy. We refer to [14–16] for the isotropic case and to [17] for the 3D case. The application of these schemes to our situation is not straightforward since they are suited to discretize the whole velocity space, without boundary conditions. Another attempt to construct an energy-conservative scheme is made in [18,19]. The authors propose a new formulation of the friction term in the Fokker–Planck equation using Maxwell stress tensor formalism. In addition they use an implicit discretization in time. The results show that energy conservation is improved over standard (particle-conservative) approaches, particularly in coarse meshes. However, generalizing this scheme for non-rectangular domains (in cylindrical coordinates) is not trivial because the discretization uses rectangular meshes with a subtle treatment of boundary terms.

It is desirable for our purpose to use a representation that can readily conform to the geometric details of the velocity domain. One candidate is a logically rectangular, nonorthogonal grid. The nodes of such a grid can be indexed the same way as a rectangular grid but the corresponding cells are quadrangles. A finite volume formulation has been the preferred technique for discretizing a problem where conservation is an important property to be modelled. Since the diffusion tensor $\boldsymbol{D}$ may be discontinuous, a cell centre finite volume algorithm has been chosen. We use a semi-implicit method to remove the time step restriction for numerical stability. The algorithm requires the evaluation of surface integrals at every point of a two-dimensional grid. For large problems, parallelization is a necessity because of storage requirements. The numerical algorithm has been implemented on a COMPAQ SC232 parallel computer.

This paper is organized as follows. In Section 2 we derive a finite volume approximation to the Fokker–Planck equation for use on a quadrangular mesh in spherical geometry. We describe our implementation of a semi-implicit time integration algorithm. In Section 3 we provide results of numerical experiments. We show the effects of various input parameters on the plasma performance (electron density, confinement time, electron mean energy and absorbed power). The results are summarized and conclusions are drawn in Section 4.

2. Approximation to the Fokker–Planck equation

2.1. The Fokker–Planck equation for the EDF

The appropriate kinetic equation for the EDF $f_e(\boldsymbol{v},t)$ is

$$\frac{\partial f_e}{\partial t} = L^{e/e}\frac{\partial}{\partial v_i}\left(f_e\frac{\partial \varphi_e}{\partial v_i}\right) + \sum_i L^{e/i}\frac{m_e}{m_i}\frac{\partial}{\partial v_i}\left(f_e\frac{\partial \varphi_i}{\partial v_i}\right) - L^{e/e}\frac{\partial}{\partial v_i}\left(\frac{\partial f_e}{\partial v_j}\frac{\partial^2 \psi_e}{\partial v_i \partial v_j}\right) - \sum_i L^{e/i}\frac{\partial}{\partial v_i}\left(\frac{\partial f_e}{\partial v_j}\frac{\partial^2 \psi_i}{\partial v_i \partial v_j}\right) + \frac{\partial}{\partial v_i}\left(D_{i,j}\frac{\partial f_e}{\partial v_j}\right) + S_i + S_e, \quad \boldsymbol{v} \in \mathscr{U}_e, \ t > 0, \tag{8}$$

where the sum is over all the ions and where the region $\mathscr{U}_e$ is (see (2)):

$$\mathscr{U}_e = \left\{\boldsymbol{v} : 1 - \mu^2 > \frac{1}{R_m}\left(1 - \frac{v_{pe}^2}{v^2}\right)\right\}. \tag{9}$$

It is necessary to specify $f_e(\boldsymbol{v},0)$ as an initial condition

$$f_e(\boldsymbol{v},0) = f_{e,0}(\boldsymbol{v}), \quad \boldsymbol{v} \in \mathscr{U}_e. \tag{10}$$

The boundary condition is

$$f_e(\boldsymbol{v},t) = 0, \quad \boldsymbol{v} \in \partial\mathscr{U}_e, \ t > 0. \tag{11}$$

The electron density is given by

$$n_e(t) = \int_{\mathscr{U}_e} f_e(\boldsymbol{v},t)\,d\boldsymbol{v}. \tag{12}$$

Concerning the source terms S_i and S_e two possible mechanisms are considered.

(1) The ionization in the volume of the plasma produces electrons as follows:

$$S_i(\boldsymbol{v},t) = n_0\chi(|\boldsymbol{v}|)\int_{\mathscr{U}_e} f_e(\boldsymbol{v}',t)\sigma_{0\to i}(|\boldsymbol{v}'|)|\boldsymbol{v}'|\,d\boldsymbol{v}'. \tag{13}$$

We have restricted ourselves to single ionization of neutrals. The ionization cross section of the atoms $\sigma_{0\to i}$ is given by Lotz in [20]. Then n_0 is the neutral density and χ is a shape function satisfying

$$\chi(v) = 0 \quad \text{if } v > v_{pe} \quad \text{and} \quad 4\pi\int_0^{v_{pe}} \chi(v)v^2\,dv = 1. \tag{14}$$

The electrons produced by ionization are cold but the exact distribution is not known: we have chosen

$$\chi(v) = c\left(\frac{v}{v_{pe}} - 1\right)^2 \quad \text{if } v \leqslant v_{pe}, \tag{15}$$

where c is a constant determined by (14).

(2) As they leave the plasma by entering the loss cone, the electrons hit the walls of the chamber. They induce secondary electrons as follows:

$$S_e(\boldsymbol{v},t) = \alpha\chi(|\boldsymbol{v}|)\left.\frac{dn_e}{dt}\right|_{lc}. \tag{16}$$

Here $\frac{\mathrm{d}n_\mathrm{e}}{\mathrm{d}t}\Big|_{\mathrm{lc}}$ stands for the electrons flux through the boundary of the loss cone:

$$\left.\frac{\mathrm{d}n_\mathrm{e}}{\mathrm{d}t}\right|_{\mathrm{lc}} = \int_{\partial\mathscr{U}_\mathrm{e}} \left(L^{\mathrm{e/e}} f_\mathrm{e} \frac{\partial \varphi_\mathrm{e}}{\partial v_i} + \sum_\mathrm{i} L^{\mathrm{e/i}} \frac{m_\mathrm{e}}{m_\mathrm{i}} f_\mathrm{e} \frac{\partial \varphi_\mathrm{i}}{\partial v_i} - L^{\mathrm{e/e}} \frac{\partial f_\mathrm{e}}{\partial v_j} \frac{\partial^2 \psi_\mathrm{e}}{\partial v_i \partial v_j} - \sum_\mathrm{i} L^{\mathrm{e/i}} \frac{\partial f_\mathrm{e}}{\partial v_j} \frac{\partial^2 \psi_\mathrm{i}}{\partial v_i \partial v_j} + D_{i,j} \frac{\partial f_\mathrm{e}}{\partial v_j} \right) n_\mathrm{i}\, \mathrm{d}S, \tag{17}$$

where $\boldsymbol{n} = (n_1, n_2, n_3)$ is the vector of unit outward normal to the boundary $\partial\mathscr{U}_\mathrm{e}$. The secondary emission coefficient α depends on the material of the wall. The secondary electrons are cold and for simplicity we use the same shape function $\chi(v)$ as for the electrons produced by ionization.

The ions are assumed to form a Maxwellian background

$$f_\mathrm{i}(\boldsymbol{v}, t) = f_\mathrm{i}(v, t) = \frac{n_\mathrm{i}(t)}{(2\pi k T_\mathrm{i}/m_\mathrm{i})^{3/2}} \mathrm{e}^{-(m_\mathrm{i}/2kT_\mathrm{i})v^2}, \tag{18}$$

where k is the Boltzmann's universal constant, T_i is the temperature and where n_i is the density for ions of species i: we assume

$$\sum_\mathrm{i} Z_\mathrm{i} n_\mathrm{i}(t) = n_\mathrm{e}(t). \tag{19}$$

Since the ionic population is Maxwellian, the ionic Rosenbluth potentials are isotropic

$$\varphi_\mathrm{i}(\boldsymbol{v}, t) = \varphi_\mathrm{i}(v, t) = -\frac{1}{v}\int_0^v f_\mathrm{i}(w, t) w^2\, \mathrm{d}w - \int_v^{+\infty} f_\mathrm{i}(w, t) w\, \mathrm{d}w = -\frac{n_\mathrm{i}(t)}{4\pi v} \mathrm{erf}\left(\left(\frac{m_\mathrm{i}}{2kT_\mathrm{i}} \right)^{1/2} v \right), \tag{20}$$

$$\begin{aligned} \psi_\mathrm{i}(\boldsymbol{v}, t) = \psi_\mathrm{i}(v, t) &= -\frac{v}{2}\int_0^v f_\mathrm{i}(w, t) w^2 \left(1 + \frac{1}{3}\frac{w^2}{v^2} \right) \mathrm{d}w - \frac{1}{2}\int_v^{+\infty} f_\mathrm{i}(w, t) w^3 \left(1 + \frac{1}{3}\frac{v^2}{w^2} \right) \mathrm{d}w \\ &= -\frac{n_\mathrm{i}(t)}{8\pi^{3/2}} \left(\frac{2kT_\mathrm{i}}{m_\mathrm{i}} \right)^{1/2} \mathrm{e}^{-(m_\mathrm{i}/2kT_\mathrm{i})v^2} - \frac{n_\mathrm{i}(t)}{8\pi} \left(v + \frac{kT_\mathrm{i}}{m_\mathrm{i} v} \right) \mathrm{erf}\left(\left(\frac{m_\mathrm{i}}{2kT_\mathrm{i}} \right)^{1/2} v \right). \end{aligned} \tag{21}$$

2.2. The spherical coordinate system

The transformation of (8) to spherical polar coordinates (v, μ) has been given by Rosenbluth et al. [4]. With our assumption of azimuthal symmetry, the equation for the EDF $f_\mathrm{e}(v, \mu, t)$ is

$$\begin{aligned} \frac{\partial f_\mathrm{e}}{\partial t} = {} & \frac{1}{v^2}\frac{\partial}{\partial v}\left(v^2 a_{vv} \frac{\partial f_\mathrm{e}}{\partial v} \right) + \frac{1}{v^2}\frac{\partial}{\partial v}\left((1-\mu^2) a_{v\mu} \frac{\partial f_\mathrm{e}}{\partial \mu} \right) + \frac{1}{v^2}\frac{\partial}{\partial \mu}\left((1-\mu^2) a_{\mu v} \frac{\partial f_\mathrm{e}}{\partial v} \right) \\ & + \frac{1}{v^2}\frac{\partial}{\partial \mu}\left(\frac{(1-\mu^2)^2}{v^2} a_{\mu\mu} \frac{\partial f_\mathrm{e}}{\partial \mu} \right) + \frac{1}{v^2}\frac{\partial}{\partial v}\left(v^2 a_v f_\mathrm{e} \right) + \frac{1}{v^2}\frac{\partial}{\partial \mu}\left((1-\mu^2) a_\mu f_\mathrm{e} \right) + S_\mathrm{i} + S_\mathrm{e}, \end{aligned} \tag{22}$$

for $(v, \mu) \in \mathscr{U}'_\mathrm{e}$, $t > 0$. Here the domain $\mathscr{U}'_\mathrm{e}$ is defined by

$$\mathscr{U}'_\mathrm{e} = \{ (v, \mu) \in (0, v_\mathrm{lim}) \times (0, 1) \ : \ \mu < \mu_\mathrm{lc}(v) \quad \text{if } v > v_\mathrm{pe} \}, \tag{23}$$

where v_lim is the light velocity and

$$\mu_\mathrm{lc}(v) = \left(1 - \frac{1}{R_\mathrm{m}} \left(1 - \frac{v_\mathrm{pe}^2}{v^2} \right) \right)^{1/2}. \tag{24}$$

This domain is shown in Fig. 3.

The initial condition (10) becomes

$$f_e(v,\mu,0) = f_{e,0}(v,\mu), \quad (v,\mu) \in \mathscr{U}'_e \tag{25}$$

and the boundary condition (11) can be written

$$f_e(v,\mu,t) = 0 \quad \text{if } v_{pe} \leqslant v \leqslant v_{lim} \text{ and } \mu = \mu_{lc}(v), \quad t > 0. \tag{26}$$

In addition we set

$$f_e(v,\mu,t) = 0 \quad \text{if } v = v_{lim}, \quad 0 \leqslant \mu \leqslant \mu_{lc}(v_{lim}), \ \ t > 0, \tag{27}$$

and

$$\frac{\partial f_e}{\partial \mu}(v,0,t) = 0, \quad \text{if } 0 \leqslant v \leqslant v_{lim}, \ \ t > 0. \tag{28}$$

The last condition is a result of the requirement that the distribution be symmetric with respect to $\mu = 0$. The coefficients $a_{vv}, a_{v\mu}, a_{\mu v}, a_{\mu\mu}$ and a_v, a_μ are given by

$$a_{vv} = -L^{e/e}\frac{\partial^2 \psi_e}{\partial v^2} - \sum_i L^{e/i}\frac{\partial^2 \psi_i}{\partial v^2} + D_{vv}, \tag{29}$$

$$a_{v\mu} = -L^{e/e}\left(\frac{\partial^2 \psi_e}{\partial v \partial \mu} - \frac{1}{v}\frac{\partial \psi_e}{\partial \mu}\right) + D_{v\mu} = a_{\mu v}, \tag{30}$$

$$a_{\mu\mu} = -L^{e/e}\left(\frac{\partial^2 \psi_e}{\partial \mu^2} + \frac{v}{1-\mu^2}\frac{\partial \psi_e}{\partial v} - \frac{\mu}{1-\mu^2}\frac{\partial \psi_e}{\partial \mu}\right) - \sum_i L^{e/i}\frac{v}{1-\mu^2}\frac{\partial \psi_i}{\partial v} + D_{\mu\mu}, \tag{31}$$

$$a_v = L^{e/e}\frac{\partial \varphi_e}{\partial v} + \sum_i L^{e/i}\frac{m_e}{m_i}\frac{\partial \varphi_i}{\partial v}, \tag{32}$$

$$a_\mu = L^{e/e}\frac{\partial \varphi_e}{\partial \mu}. \tag{33}$$

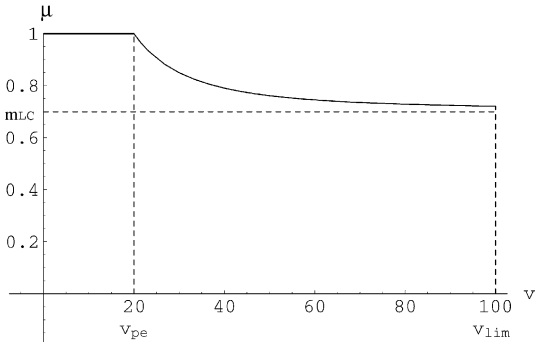

Fig. 3. Velocity domain $\mathscr{U}'_e$.

Here the Rosenbluth potentials can be given in terms of two-dimensional integrals

$$\varphi_e(v,\mu,t) = -\frac{1}{2\pi}\int_{\mathscr{U}'_e} f_e(v',\mu',t)\Lambda^{\star}(v',\mu';v,\mu)\,\mathrm{d}\mu' v'^2\,\mathrm{d}v', \tag{34}$$

$$\psi_e(v,\mu,t) = -\frac{1}{4\pi}\int_{\mathscr{U}'_e} f_e(v',\mu',t)\Omega^{\star}(v',\mu';v,\mu)\,\mathrm{d}\mu' v'^2\,\mathrm{d}v', \tag{35}$$

with $\Lambda^{\star}$ and $\Omega^{\star}$ defined in terms of the complete elliptic integrals K and E (see [21]) as follows:

$$\Lambda^{\star}(v',\mu';v,\mu) = \frac{1}{2}\big(\Lambda(v',\mu';v,\mu) + \Lambda(v',-\mu';v,\mu)\big), \tag{36}$$

$$\Omega^{\star}(v',\mu';v,\mu) = \frac{1}{2}\big(\Omega(v',\mu';v,\mu) + \Omega(v',-\mu';v,\mu)\big), \tag{37}$$

$$\Lambda(v',\mu';v,\mu) = \frac{4}{x(v',\mu';v,\mu)}K\big(y(v',\mu';v,\mu)\big), \tag{38}$$

$$\Omega(v',\mu';v,\mu) = 4x(v',\mu';v,\mu)E\big(y(v',\mu';v,\mu)\big), \tag{39}$$

$$x(v',\mu';v,\mu) = \left(v^2 + v'^2 - 2vv'\left(\mu\mu' - \sqrt{1-\mu^2}\sqrt{1-\mu'^2}\right)\right)^{1/2}, \tag{40}$$

$$y(v',\mu';v,\mu) = \frac{\left(4vv'\sqrt{1-\mu^2}\sqrt{1-\mu'^2}\right)^{1/2}}{x(v',\mu';v,\mu)}. \tag{41}$$

Evaluation of the coefficients defined in (29)–(33) requires derivatives of the Rosenbluth potentials. The derivatives of φ_i and ψ_i may be obtained through differentiation of (20) and (21). To obtain derivatives of φ_e and ψ_e requires differentiation of $\Lambda(v',\mu';v,\mu)$ and $\Omega(v',\mu';v,\mu)$ with respect to v and μ. This is done analytically.

The formulas for the components of the diffusion tensor $\boldsymbol{D}$ in spherical coordinates are given in the book of Killeen et al. [11]. We focus on whistler wave electron cyclotron resonance (ECR) heating in mirror geometry, as the wave is injected parallel to the magnetic axis, which favours its coupling to the whistler mode. Bernstein wave heating is not considered here, as this would require a perpendicular launching of the wave. Additionally we only consider the fundamental resonance. In this setting, we obtain

$$D_{vv} = D\xi(1-\mu^2)\frac{\tau_c^2}{\tau_B}, \tag{42}$$

$$D_{v\mu} = -D\frac{v\sqrt{1-\xi(1-\mu^2)}}{\mu}\left(\sqrt{1-\xi(1-\mu^2)} + \frac{v}{v_\phi}\right)\frac{\tau_c^2}{\tau_B} = D_{\mu v}, \tag{43}$$

$$D_{\mu\mu} = D\frac{1-\xi(1-\mu^2)}{\xi\mu^2}\frac{v^2}{1-\mu^2}\left(\sqrt{1-\xi(1-\mu^2)} + \frac{v}{v_\phi}\right)^2\frac{\tau_c^2}{\tau_B}. \tag{44}$$

Here the quantity D is given by

$$D = \frac{e^2}{4m_e^2} E^2, \tag{45}$$

where E is the amplitude of the fluctuating RF electric field,

$$\xi = \frac{B_{res}}{B_{min}}, \tag{46}$$

where B_{res} is the magnetic induction evaluated at the resonance, which gives

$$\xi = \xi_0 + \frac{v}{v_\phi}\xi_0 \left(-\xi_0 \frac{1-\mu^2}{2}\frac{v}{v_\phi} + \sqrt{\left(\xi_0 \frac{1-\mu^2}{2}\frac{v}{v_\phi}\right)^2 + 1 - \xi_0(1-\mu^2)} \right) \tag{47}$$

with

$$\xi_0 = \frac{B_0}{B_{min}} \quad \text{and} \quad B_0 = \frac{m_e 2\pi f}{e}, \tag{48}$$

f being the frequency of the wave and v_ϕ being the phase velocity of the wave. Additionally τ_c is the effective correlation time,

$$\tau_c^2 = 2\pi \left(\frac{ev}{m_e} \left(\frac{v\xi_0(1-\mu^2)}{2v_\phi} + \sqrt{1-\xi(1-\mu^2)} \right) \right)^{-1} \left(\left(\frac{\partial B}{\partial z} \right)_{res} \right)^{-1}, \tag{49}$$

where $(\partial B/\partial z)_{res}$ is the gradient of the magnetic field at the resonance. The following parabolic profile is used:

$$B(z) = B_{min}\left(1 + \frac{4z^2}{L^2}\right), \tag{50}$$

where B_{min} corresponds to the center of the mirror and L is a characteristic length of the magnetic field: this formula is a good approximation of the true field. It follows

$$\left(\frac{\partial B}{\partial z} \right)_{res} = \frac{4B_{min}}{L}\sqrt{\xi - 1}. \tag{51}$$

Finally τ_B is the bounce-period and satisfies in this case

$$\tau_B = \begin{cases} \frac{\pi L}{v\sqrt{1-\mu^2}} & \text{if } \mu \leqslant \mu_{LC}, \\ \frac{2L}{v\sqrt{1-\mu^2}} \arcsin\sqrt{(R_m - 1)\frac{1-\mu^2}{\mu^2}} & \text{if } \mu > \mu_{LC}. \end{cases} \tag{52}$$

The main feature of ECR heating is the resonant interaction between electrons and the RF wave. Only the electrons passing through the resonant region are heated and diffused by the RF wave. Therefore the RF diffusion coefficients are taken to be zero for $\mu < \mu_1 = \sqrt{1 - 1/\xi_0}$. Some resonant processes are still possible in the region $B < B_0$ or $\mu < \mu_1$, like tangent resonance (see [11]); they are not considered in the present paper since we assume that the RF wave is completely absorbed in the region $B > B_0$ (see [24]).

2.3. Velocity discretization

We wish to solve Eq. (22) in the domain $\mathscr{U}'_e$. We do this by converting the integro-differential equation to an algebraic equation using a finite volume method in velocity space and a semi-implicit scheme in time.

First, we establish a logically rectangular grid by dividing v and μ into J and L pieces, respectively (see Fig. 4). Since the RF diffusion coefficients are set to zero for $\mu < \mu_1$, the line $\mu = \mu_1$ is a grid line. On the domain $0 \leqslant v \leqslant v_{\lim}$ we have a mesh denoted by $v_{j+1/2},\ 0 \leqslant j \leqslant J$. On each interval $[0, \min(\mu_{\mathrm{lc}}(v_{j+1/2}), 1)]$ we use a mesh denoted by $\mu_{\ell+1/2}^{j+1/2},\ 0 \leqslant \ell \leqslant L$.

The quadrangle defined by the nodes

$$\left(v_{j-1/2}, \mu_{\ell-1/2}^{j-1/2}\right), \quad \left(v_{j-1/2}, \mu_{\ell+1/2}^{j-1/2}\right), \quad \left(v_{j+1/2}, \mu_{\ell-1/2}^{j+1/2}\right), \quad \text{and} \quad \left(v_{j+1/2}, \mu_{\ell+1/2}^{j+1/2}\right)$$

is called $Q_{j,\ell}$. We define

$$v_j = \frac{1}{2}\left(v_{j-1/2} + v_{j+1/2}\right), \tag{53}$$

$$\mu_{\ell+1/2}^{j} = \frac{1}{2}\left(\mu_{\ell+1/2}^{j-1/2} + \mu_{\ell+1/2}^{j+1/2}\right), \quad \mu_{\ell}^{j+1/2} = \frac{1}{2}\left(\mu_{\ell-1/2}^{j+1/2} + \mu_{\ell+1/2}^{j+1/2}\right), \tag{54}$$

$$\mu_{j,\ell} = \frac{1}{4}\left(\mu_{\ell-1/2}^{j-1/2} + \mu_{\ell+1/2}^{j-1/2} + \mu_{\ell-1/2}^{j+1/2} + \mu_{\ell+1/2}^{j+1/2}\right), \tag{55}$$

$$\delta v_j = v_{j+1/2} - v_{j-1/2}, \tag{56}$$

$$\delta\mu_{\ell+1/2}^{j} = \mu_{\ell+1/2}^{j+1/2} - \mu_{\ell+1/2}^{j-1/2}, \quad \delta\mu_{\ell}^{j+1/2} = \mu_{\ell+1/2}^{j+1/2} - \mu_{\ell-1/2}^{j+1/2}. \tag{57}$$

Following the method presented in [22], we construct the finite volume approximation by integrating (22) over each cell and using Gauss' Theorem to convert integrals over cells into integrals over cell boundaries. This procedure allows exact conservation of particles. However energy conservation is not guaranteed. It is shown in [19] that energy conservation in an energy-conservative algorithm is better than in a particle-conservative, non-energy-conservative scheme, but the advantage may be lost in fine meshes. Our algorithm is well-adapted to parallel computers (see below) and this allows mesh refinement. We use a semi-implicit method for time integration. If the time step is Δt, then $t_n = n\Delta t$ and $f_{j,\ell}^n$ is the approximation to the EDF at the center $\boldsymbol{p}_{j,\ell} = (v_j, \mu_{j,\ell})$ of the cell $Q_{j,\ell}$ at time t_n. We write

$$\frac{\omega_{j,\ell}}{\Delta t}\left(f_{j,\ell}^{n+1} - f_{j,\ell}^{n}\right) = \phi_{j,\ell+1/2}^{j,\ell,n+1} - \phi_{j,\ell-1/2}^{j,\ell,n+1} + \phi_{j+1/2,\ell}^{j,\ell,n+1} - \phi_{j-1/2,\ell}^{j,\ell,n+1} + \omega_{j,\ell} S_{j,\ell}^{n}. \tag{58}$$

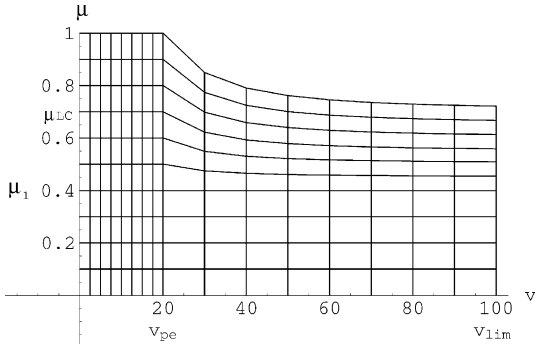

Fig. 4. The numerical grid.

Here $\omega_{j,\ell}$ is the volume of the cell $Q_{j,\ell}$:

$$\omega_{j,\ell} = \int_{Q_{j,\ell}} v^2 \,\mathrm{d}v\,\mathrm{d}\mu, \tag{59}$$

and

$$\phi^{j,\ell,n+1}_{j,\ell+1/2} = \left(\boldsymbol{u}^{j,\ell,n}_{j,\ell+1/2}\cdot\nabla + \alpha^n_{j,\ell+1/2}\right) f_{\mathrm{e}}^{j,\ell,n+1}(\boldsymbol{p}_{j,\ell+1/2}), \tag{60}$$

$$\phi^{j,\ell,n+1}_{j+1/2,\ell} = \left(\boldsymbol{u}^{j,\ell,n}_{j+1/2,\ell}\cdot\nabla + \alpha^n_{j+1/2,\ell}\right) f_{\mathrm{e}}^{j,\ell,n+1}(\boldsymbol{p}_{j+1/2,\ell}), \tag{61}$$

$$S^n_{j,\ell} = S^n_{\mathrm{i}}(v_j) + S^n_{\mathrm{e}}(v_j), \tag{62}$$

where

$$\begin{aligned}\boldsymbol{u}^{j,\ell,n}_{j,\ell+1/2} = \Bigg(& -\delta\mu^j_{\ell+1/2}\left(v^2 a^{j,\ell,n}_{vv}\right)(\boldsymbol{p}_{j,\ell+1/2}) + \delta v_j\left((1-\mu^2)a^{j,\ell,n}_{\mu v}\right)(\boldsymbol{p}_{j,\ell+1/2}),\\ & -\delta\mu^j_{\ell+1/2}\left((1-\mu^2)a^{j,\ell,n}_{v\mu}\right)(\boldsymbol{p}_{j,\ell+1/2}) + \delta v_j\left(\frac{(1-\mu^2)^2}{v^2}a^{j,\ell,n}_{\mu\mu}\right)(\boldsymbol{p}_{j,\ell+1/2})\Bigg),\end{aligned} \tag{63}$$

$$\boldsymbol{u}^{j,\ell,n}_{j+1/2,\ell} = \delta\mu^{j+1/2}_{\ell}\left(\left(v^2 a^{j,\ell,n}_{vv}\right)(\boldsymbol{p}_{j+1/2,\ell}), \left((1-\mu^2)a^{j,\ell,n}_{v\mu}\right)(\boldsymbol{p}_{j+1/2,\ell})\right), \tag{64}$$

$$\alpha^n_{j,\ell+1/2} = -\delta\mu^j_{\ell+1/2}(v^2 a^n_v)(\boldsymbol{p}_{j,\ell+1/2}) + \delta v_j\left((1-\mu^2)a^n_\mu\right)(\boldsymbol{p}_{j,\ell+1/2}), \tag{65}$$

$$\alpha^n_{j+1/2,\ell} = \delta\mu^{j+1/2}_{\ell}(v^2 a^n_v)(\boldsymbol{p}_{j+1/2,\ell}), \tag{66}$$

and

$$\boldsymbol{p}_{j,\ell+1/2} = \left(v_j, \mu^j_{\ell+1/2}\right), \quad \boldsymbol{p}_{j+1/2,\ell} = \left(v_{j+1/2}, \mu^{j+1/2}_{\ell}\right). \tag{67}$$

Here the coefficients $a_{vv}, a_{v\mu}, a_{\mu v}, a_{\mu\mu}$ and a_v, a_μ are computed at time t_n. Since the components of the diffusion tensor $\boldsymbol{D}$ are discontinuous, the mesh cell indices j,ℓ indicate that the corresponding coefficient uses the values of $\boldsymbol{D}$ on the cell $Q_{j,\ell}$. Next we must specify the way in which the combinations of f_{e} and its derivatives are to be computed at the edges of the cells in terms of the values of f_{e} at the centers of the cells.

We start with horizontal edges. Let $\boldsymbol{p}_{\mathrm{down}}$ be the point where the half-line $\boldsymbol{p}_{j,\ell+1/2} - s\boldsymbol{u}^{j,\ell,n}_{j,\ell+1/2},\ s>0$ intersects one edge of the hexagon of vertices $\boldsymbol{p}_{j-1,\ell}, \boldsymbol{p}_{j,\ell}, \boldsymbol{p}_{j+1,\ell}, \boldsymbol{p}_{j+1,\ell+1}, \boldsymbol{p}_{j,\ell+1}$ and $\boldsymbol{p}_{j-1,\ell+1}$. The value f^{n+1}_{down} of f_{e} at $\boldsymbol{p}_{\mathrm{down}} = \boldsymbol{p}_{j,\ell+1/2} - s_{\mathrm{down}}\boldsymbol{u}^{j,\ell,n}_{j,\ell+1/2}$ is approximated by a linear combination of the values of f_{e} at the neighbouring vertices. The term $\phi^{j,\ell,n+1}_{j,\ell+1/2}$ is discretized as follows:

$$\phi^{j,\ell,n+1}_{j,\ell+1/2} \approx \frac{f^{j,\ell,n+1}_{j,\ell+1/2} - f^{n+1}_{\mathrm{down}}}{s_{\mathrm{down}}} + \alpha^n_{j,\ell+1/2} f^{j,\ell,n+1}_{j,\ell+1/2}. \tag{68}$$

The formula for $\phi^{j,\ell+1,n+1}_{j,\ell+1/2}$ is similar:

$$\phi^{j,\ell+1,n+1}_{j,\ell+1/2} \approx \frac{f^{n+1}_{\mathrm{up}} - f^{j,\ell+1,n+1}_{j,\ell+1/2}}{s_{\mathrm{up}}} + \alpha^n_{j,\ell+1/2} f^{j,\ell+1,n+1}_{j,\ell+1/2}. \tag{69}$$

The values $f^{j,\ell,n+1}_{j,\ell+1/2}, f^{j,\ell+1,n+1}_{j,\ell+1/2}$ and $\phi^{j,\ell,n+1}_{j,\ell+1/2}, \phi^{j,\ell+1,n+1}_{j,\ell+1/2}$ are obtained by adding continuity requirements:

$$f^{j,\ell,n+1}_{j,\ell+1/2} = f^{j,\ell+1,n+1}_{j,\ell+1/2}, \tag{70}$$

$$\phi^{j,\ell,n+1}_{j,\ell+1/2} = \phi^{j,\ell+1,n+1}_{j,\ell+1/2}. \tag{71}$$

Fig. 5 illustrates the scheme.

The discretization on vertical edges is similar. Boundary conditions slightly modify the preceding algorithm.

The expressions for the coefficients $(1-\mu^2)a^n_\mu$ through $v^2 a^{j,\ell,n}_{vv}$ are complicated and these coefficients must be evaluated at the edges of the cells in terms of the values $f^n_{j,\ell}$. The computation of these coefficients represents a high percentage of the total number of operations required. Since the structure of each of the five coefficients is quite similar, we only consider the detailed evaluation of one of them. We approximate

$$\left((1-\mu^2)a^n_\mu\right)(\boldsymbol{p}_{j,\ell+1/2}) \approx -\frac{L^{e/e}}{2\pi}\sum_{k,m} \Lambda\mu^{k,m}_{j,\ell+1/2} f^n_{k,m}, \tag{72}$$

where

$$\Lambda\mu^{k,m}_{j,\ell+1/2} = \int_{Q_{k,m}} \left((1-\mu^2)\frac{\partial \Lambda^{\star}}{\partial \mu}\right)\left(v',\mu';v_j,\mu^j_{\ell+1/2}\right) \mathrm{d}\mu' v'^2 \,\mathrm{d}v'. \tag{73}$$

Since the integrands have a relatively low degree of regularity, a quasi-Monte Carlo (QMC) method was chosen to compute the integrals. The accuracy of a QMC method with N points is $\mathcal{O}(\log(N)/N)$, which can be compared (in case of smooth functions) with the accuracy of a compound trapezoidal rule (see [23]). The calculation is easily parallelized. The device is taken to propagate primarily in the v direction, and this choice necessitates the use of many more computation cells in the v direction than in the μ direction. A parallel decomposition is performed in the v direction. The computational domain is partitioned into N_{pro} subdomains, where N_{pro} is the number of processors, and each subdomain is assigned to a processor. Each processor holds coefficients $\Lambda\mu^{k,m}_{j,\ell+1/2}$ for indices j belonging to the corresponding sudomain. In every time step each processor can compute the coefficient $((1-\mu^2)a^n_\mu)(\boldsymbol{p}_{j,\ell+1/2})$ on edge centers $\boldsymbol{p}_{j,\ell+1/2}$ interior to the processor's computational area. This step does not involve any communication among the processors and is

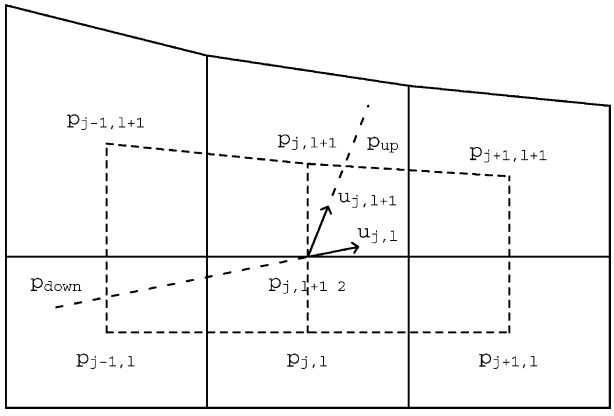

Fig. 5. The discretization on an horizontal edge.

therefore performed in parallel. Second, after each processor completes its task, interprocessor communications are performed and all the approximations $f_{j,\ell}^{n+1}$ are computed concurrently on all processors.

3. Computational results and discussion

In order to validate the numerical method, we first solve a simplified problem. We consider a plasma of electrons and Helium ions. Both populations are Maxwellian. There is no heating, and no source term. The plasma potential is set to a high value (500 V), so that the electron losses are negligible. The ion temperature T_i is taken to 200 eV. The initial electron temperature is $T_e(t=0) = 5$ eV. The temperature T_e is changing, due to interaction with ions. The theoretical equation approximating the evolution of T_e is given in [3]:

$$\frac{dT_e}{dt} = \gamma \frac{T_i - T_e}{(T_e + T_i m_e/m_i)^{3/2}}, \tag{74}$$

with some constant γ. Comparison between this solution and the results of computation is given in Fig. 6: we see that the computed values converge towards the theoretical temperature as the mesh is refined in v. No influence of the mesh size in μ was observed.

The algorithm described above has been applied to a typical ECRIS plasma calculation. Helium was chosen as the neutral gas: the ionization source is described by (13), where the value of $\sigma_{He\to He^+}$ is taken in [20]. The neutrality condition $n_i(t) = n_e(t)$ is assumed to be satisfied throughout the simulation. Losses and confinement times are computed only for electrons. In order to account for the ambipolar nature of losses in a real mirror plasma, a fixed ambipolar electrostatic potential (plasma potential) Φ was imposed retarding the electrons. For calculating the RF diffusion coefficients B_{min} was fixed at 0.435 T and L was fixed to be equal to 0.3 m in (50). The frequency f of the wave was fixed to 18 GHz.

The numerical grid consists of 200 meshes in v and 40 meshes in μ. The v-mesh was taken to be uniform between 0 and v_{pe} (100 meshes). The μ-mesh was taken to be uniform between 0 and μ_1 (15 meshes) and between μ_1 and 1 (25 meshes): see Fig. 4. With the use of the semi-implicit method the algorithm becomes stable; the time step was usually chosen to be $\Delta t = 10^{-4}$ s. It was found that smaller time steps do not change the results for the stationary state. The typical input parameters are listed in Table 1. Fig. 7 depicts the influence of the mesh size on the evolution of electron density in time. The mesh choice 200×40 appears to be a compromise between accuracy and cost, since finer grids result in minor improvements.

We study the effect of changing one of these parameters on the plasma performance, i.e., the electron density n_e, the confinement time

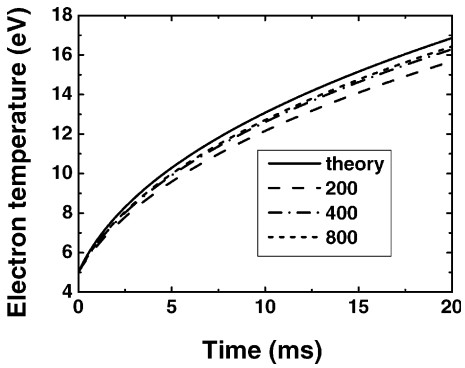

Fig. 6. Evolution of electron temperature in time: convergence with the mesh size.

Table 1
Physical dimensions for ECRIS simulations

Symbol	Description	Value
N_0	Time independent neutral (He) density	4×10^{11} cm^{-3}
E	RF electric field of the pumping wave	3000 V/m
Φ	Plasma potential	20 V
α	Secondary emission coefficient	0.1
R_m	Magnetic mirror ratio	2
v_ϕ	RF wave phase velocity	10^{10} cm/s

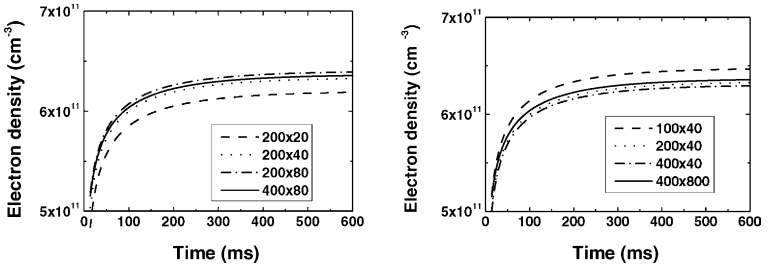

Fig. 7. Evolution of electron density in time: influence of the mesh size.

$$\tau_e = \frac{n_e}{\left.\frac{dn_e}{dt}\right|_{lc}}, \tag{75}$$

the electron mean energy ε and the absorbed power P_e (that is the power evacuated by electrons through the loss cone).

3.1. Influence of the RF wave electromagnetic field

Plasma heating and ionization of neutrals strongly depend on the diffusion of electrons in the velocity space. The diffusion caused by the RF electromagnetic field dominates the diffusion due to collisions in a wide range of RF electric field values. In Fig. 8 we show the behaviour of the electron density, confinement time, electron mean energy and absorbed power as the amplitude of the RF wave electric field is varied. In Fig. 8(a) we see that the electron density first increases, then saturates, and finally decreases: the particles are more and more efficiently heated as the input power is increased, but they are also scattered into the loss

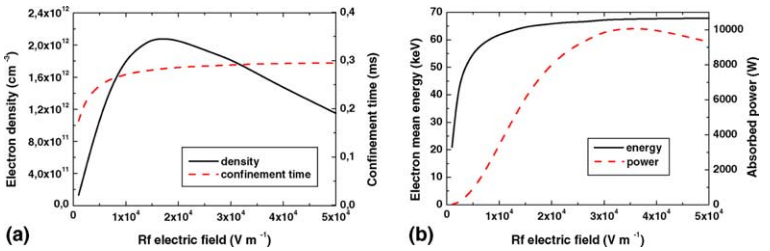

Fig. 8. (a) Electron density and confinement time, (b) electron mean energy and absorbed power as functions of the RF wave electric field.

cone with more and more efficiency, thus limiting the performance of the source. In Fig. 8(b) we observe the same behaviour for the absorbed power; however, the maximum of the absorbed power is reached at a value higher than the maximum of the density, since the power is a second order momentum of the EDF, while the density is a first order momentum. The saturation of the performance is always observed in an ECRIS. Fig. 8(b) also indicates the influence of the RF power on the electron mean energy. It rapidly increases and then saturates: as the RF power increases, the electrons created by ionization are rapidly heated and lost at high energy and they do not contribute to any increase of density or energy. This rapid saturation was observed in the experiments [25,26]. The confinement time, as shown in Fig. 8(a), has a behaviour and a typical value consistent with these experiments.

In Fig. 9 we show the change of the EDF with time. The initial distribution is Maxwellian, at a temperature of 15 eV and a density of 10^9 cm^{-3}. We choose a time step $\Delta t = 10^{-5}$ s. The results at $t = 2 \times 10^{-3}$ s are shown in Fig. 9(a). We see a strong electron diffusion in the resonance region. The steady-state EDF is shown in Fig. 9(b): we see that the collisional diffusion establishes a quasi-homogeneous angle distribution in the region $\mu < \mu_1$, which is not influenced by the RF field, while the overall shape of the EDF in the region $\mu > \mu_1$ does not change as the calculation proceeds, since the resonant RF diffusion dominates here.

In order to compare the results given by the present 2D algorithm with those given by a previous 1D method [6], we have performed 1D calculations with the same input parameters. The results of Fig. 10 are in good qualitative agreement with those described in Fig. 8. The explanation of the quantitative differences is clearly shown in Fig. 9. In contrast with what happens in 1D computations, in 2D calculations only a part of the electrons is involved in RF resonant diffusion. Consequently, the same results are obtained with larger electric fields. From this results that the absorbed power derived in the 2D code is smaller than in the

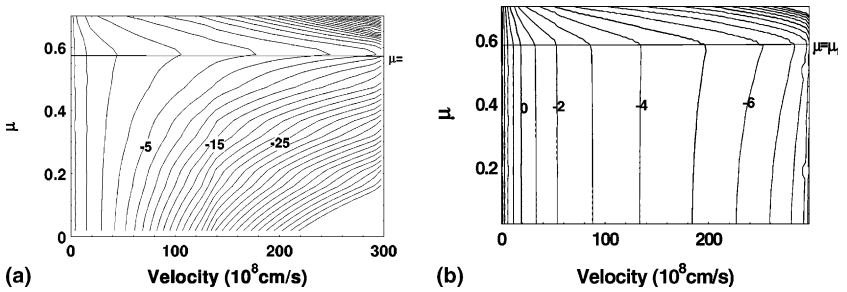

Fig. 9. (a) Contours of the EDF at $t = 2 \times 10^{-3}$ s, (b) contours of the steady-state EDF, both in logarithmic scale.

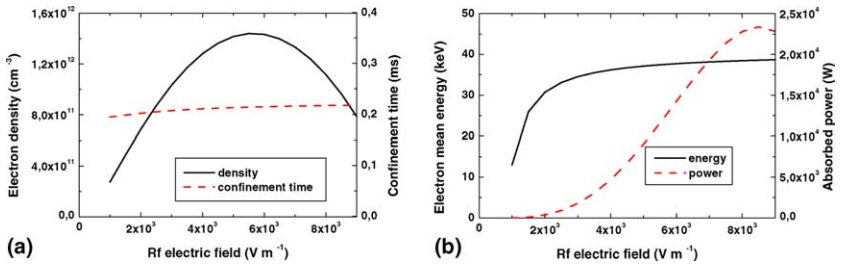

Fig. 10. 1D computations: (a) electron density and confinement time, (b) electron mean energy and absorbed power as functions of the RF wave electric field.

1D calculations. In the next sections, we present results of computations when other parameters are varied. They are also in good qualitative agreement with the results of 1D computations. It is interesting to observe that the electron confinement times computed by 1D and 2D simulations are rather close from each other, in the range of weak RF electric fields: see Fig. 11. This is due to the fact that the Coulomb collisional losses for $v \approx v_{pe}$ exceed the RF losses for $v \approx v_{\phi}$: see [27]. A simple estimation of the collisional lifetime, given in the same reference, agrees well with our computed electron confinement time.

3.2. Influence of the mirror ratio, the neutral density and the RF wave frequency

Fig. 12(a) shows the increase of density and confinement time when the mirror ratio is increased, all other parameters being kept constant. The mirror ratio is varied by changing B_{max}. The order of magnitude of the confinement time is in good agreement with the measurements already presented in [27]. In Fig. 12(b) the electron mean energy is shown to increase with increasing mirror ratio, which is normal, as the loss term is reduced. The same figure shows the power absorbed by the electrons, versus the mirror ratio: this power is low when the mirror ratio is low because the density of the plasma created is low, and it increases at higher mirror ratios as the density and energy increase. All these results are similar to those we obtained using a 1D simulation [6]. In the 2D case, the steady-state values are more sensitive to the mirror ratio: this could be explained by the fact that the electron losses through the loss cone are more accurately described by the 2D simulation. There is also another reason: in the 2D case the B_{min} and B_0 are fixed while B_{max} is varied; this is done in order to obtain the same gradient of the steady state magnetic field at the resonance. Consequently, the mirror ratio R_m is varied, while the ratio $\xi_0 = B_0/B_{min}$ is kept constant: only the upper

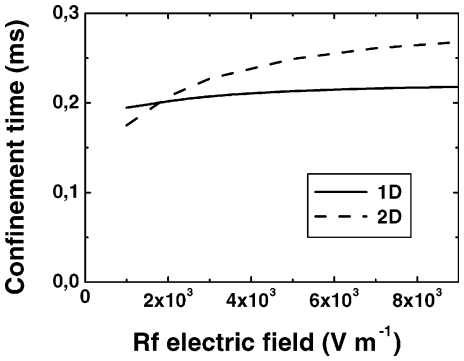

Fig. 11. Confinement time: comparison between 1D and 2D computations.

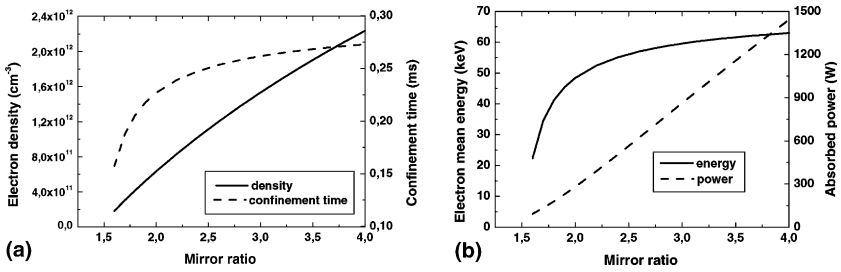

Fig. 12. (a) Electron density and confinement time, (b) electron mean energy and absorbed power as functions of the mirror ratio.

part of the velocity domain is changed (see Fig. 3). In the limiting case, when R_m only slightly differs from ξ_0, the electrons are heated very close to the loss cone boundary.

Fig. 13(a) shows the behaviour of the electron density and confinement time as the neutral density is varied. We see that the electron density monotonically increases as the neutral gas pressure increases. Such a behaviour was observed in the Quadrumafios source [27]. We also see that the higher the neutral density, the lower the confinement time, which explains why it is necessary to work at low neutral pressure to obtain multiply charged ions (MCI). A similar behaviour was predicted using the 1D-code [6, Fig. 6]. The value of the confinement time obtained (at low neutral density) is in very good agreement with the experimental results obtained in [27], and with the values of the experimental ionic confinement times presented in [28]. Fig. 13(b) shows the dependence of the mean energy and absorbed power on the neutral pressure: the higher the neutral pressure, the lower the mean energy; in order to produce high charges it is necessary to have large electron energies to overcome the ionization potentials and highly energetic electrons can only be produced at low pressures. These results are consistent with results of the 1D-code.

For the next simulations, the phase velocity of the RF wave is no longer kept constant, but is related to the plasma parameters as follows:

$$\frac{v_\phi}{c} = \left(1 + \left(\frac{f_{pe}^2}{f^2}\frac{c}{v_T}\right)^{2/3}\right)^{-1/2}, \tag{76}$$

where $f_{pe}^2 \propto n_e$ is the electron plasma frequency and v_T is an efficient electron thermal velocity (in practice, v_T is deduced from the electron mean energy). We have slightly modified the expression for v_ϕ given in [6], taking into account that v_ϕ tends to c as n_e goes to zero. Eq. (76) is added into the code, so that the phase velocity becomes a function of the other plasma quantities. Fig. 14(a) shows the electron density and confinement time versus RF frequency. The electron mean energy and the absorbed power are shown in

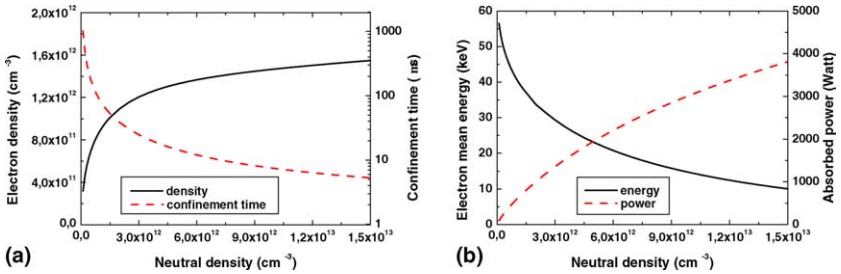

Fig. 13. (a) Electron density and confinement time, (b) electron mean energy and absorbed power as functions of the neutral density.

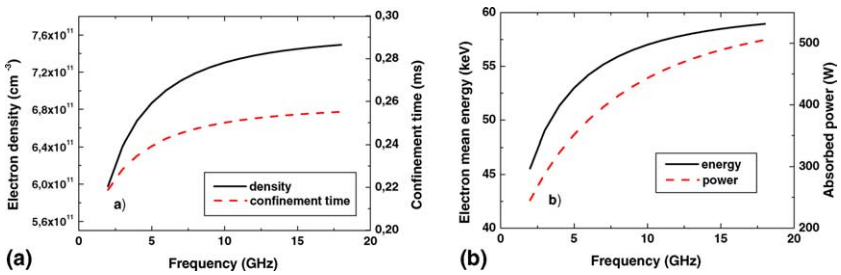

Fig. 14. (a) Electron density and confinement time, (b) electron mean energy and absorbed power as functions of the RF frequency.

Fig. 14(b). These two figures show that high frequencies are well suited to the production of multiply charged ions. These results are also consistent with 1D-results, but, again, with absolute values slightly different. This shows again that the two codes are in qualitative agreement between each other, and also consistent with the experiments.

3.3. Influence of the plasma potential and of the coefficient of secondary emission

The plasma potential is not an input parameter for the experimentalist. Physically the plasma potential is automatically established from the quasi-neutrality condition or, in the steady-state case, by equating electron and ion losses. Therefore, in our calculations, the main role of the plasma potential is to regulate electron losses in the following manner: the electrostatic potential confines all the electrons with energy smaller than $e\Phi$ independently from the pitch angle. Moreover, even for electrons with higher energy, the plasma potential facilitates the confinement by lowering their longitudinal velocity. As a result the loss cone is modified: see Fig. 3.

In Fig. 15 we show the behaviour of the electron density, confinement time, electron mean energy and absorbed power as the plasma potential is artificially changed. Different values of plasma potential can be considered as reflecting different physical situations, for example different types of neutral gas used. We see that increasing the plasma potential causes an increase of the electron density as a consequence of a better electron confinement in the region of large ionization cross section (close to the plasma potential). On the other side, the higher the potential the higher the ratio of electrons of low energy in the distribution. Therefore, the electron mean energy and electron confinement time decrease as a consequence of higher collisional rate in the low energy region.

We see almost the same behaviour in Fig. 16, which shows the variation of the electron density, confinement time, electron mean energy and absorbed power as the coefficient α is changed. The secondary

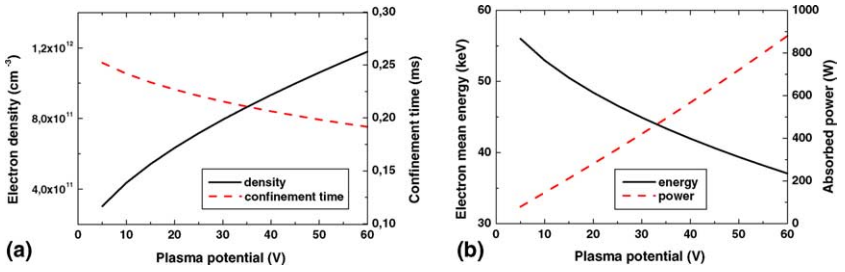

Fig. 15. (a) Electron density and confinement time, (b) electron mean energy and absorbed power as functions of the plasma potential.

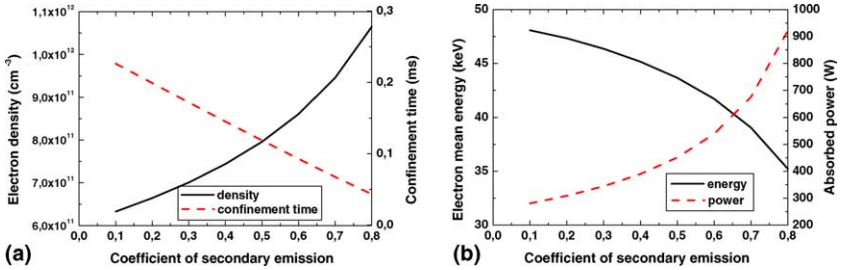

Fig. 16. (a) Electron density and confinement time, (b) electron mean energy and absorbed power as functions of the secondary emission coefficient.

emission acts like a pump: it gives back lost electrons, which have already been heated, to the low energy part of the EDF. In contrast to the plasma potential, the coefficient of secondary emission can be changed by technical means (for example by changing the material of the walls).

3.4. Afterglow

At the end of the heating process, near steady-state, the RF wave electric field sustains an EDF which is far from being Maxwellian, as demonstrated in Fig. 9(b). The EDF is approximately isotropic for $\mu < \mu_1$ and abruptly falls beyond μ_1. Assuming a short relaxation time, based on the effective electron–ion collision time (see [3]):

$$\tau_{ei} = \frac{\sqrt{m_e}}{\pi\sqrt{2}\lambda n_i Z_i^2 e^4}\left(\frac{m_e v^2}{2}\right)^{3/2}, \tag{77}$$

one can guess a rapid filling of the region $\mu > \mu_1$ by the electrons when the RF field is turned off; and as a consequence of the higher electron density near the loss cone boundary, electron losses will increase. We have modeled this situation and the results are depicted in Fig. 17: the time step was $\Delta t = 10^{-6}$ s. The plasma is first heated by a RF electric field of 3000 V/m and reaches steady-state. At $t = 100.2$ ms the electric field falls down exponentially with a characteristic time of 30 μs. The characteristic electron pitch angle diffusion time τ_{ei} is approximately 10 μs for 100 eV electrons. We see that during a short time interval of ~ 10 μs, electron losses fall down: that can be attributed to instantaneous drop of electron losses due to scattering in the loss cone by the RF wave for $v \approx v_\phi$. Then, electron losses increase during ~ 20 μs, that is until the RF wave disappears. This increase is due to strong electron diffusion towards the region $\mu > \mu_1$. The second peak of electron losses at $t = 100.4$ ms can be explained by a more efficient ionization in the low energy region after turning off the RF power. This change in electron losses will affect the ion losses because of the necessary neutrality of the plasma and ion losses are proportional to ion current. This increase of the electron losses is similar to the well known increase of ion current (afterglow) produced under similar conditions: see [29]. We think that it may be the same phenomenon despite the short impulse duration (in comparison with the ion current impulse duration). The difference can be explained by the delayed ion response to electron losses: electron losses are governed by fast processes like pitch angle diffusion and the falling of the RF power, while the ion characteristic time is determined by the collisional diffusion in the physical space. Note that He^+ ions were used in the computations: a higher peak of electron losses can be expected in the case of ions with larger Z_is.

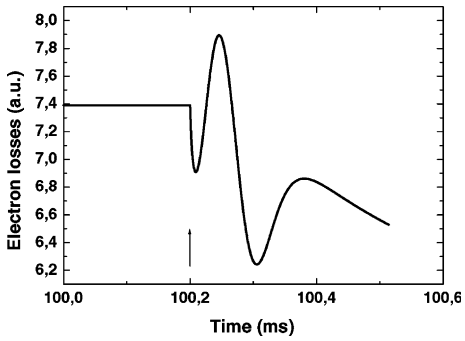

Fig. 17. The time evolution of electron losses as the RF electric field is turned off (arrow).

4. Conclusions

We have presented a new version of a Fokker–Planck code adapted to the physics of ECR plasmas. This code uses a new method for the resolution of the full integro-differential Fokker–Planck equation with a quasilinear heating term, well adapted to a parallel computer. This code shows the same qualitative results of our earlier 1D code, which is a new validation of the results obtained with that older code. However this code is much more powerful: (i) the values of the absorbed RF power derived with the 2D code are much closer to the experimental values, as the EDF is described much more precisely; (ii) the sensitivity of the results with the mirror ratio is much greater, which is again consistent with experimental results; (iii) it is shown that the position of the resonant field with respect to the minimum and maximum magnetic field influences the results, as also observed. The influence of the (fixed) plasma potential has been studied. Eventually, a kind of afterglow effect has been discovered, which may be related to the observed enhancement of the ionic current as the RF is switched off. Nevertheless the present code does not permit the calculation of the ion charge-state distribution. For doing this, it is required to compute the time evolution of the ionic population. The next step of the modelisation should be the development of a fully self-consistent (i.e. with a variable plasma potential) code for the calculation of the performances of ECRIS.

Acknowledgements

We acknowledge the support of INTAS (Project No. 01-0373).

References

[1] R. Geller, Electron Cyclotron Resonance Ion Sources and ECR Plasmas, Institute of Physics Publishing, Bristol/Philadelphia, 1996.
[2] A. Girard, G. Melin, ECR ion sources today. Physics, performance and technology, Nucl. Instr. Meth. Phys. Res. A 382 (1996) 252.
[3] L. Spitzer Jr., Physics of Fully Ionized Gases, second ed., Wiley/Interscience, New York, 1962.
[4] M.N. Rosenbluth, W.M. MacDonald, D.L. Judd, Fokker–Planck equation for an inverse-square force, Phys. Rev. 107 (1957) 1.
[5] B.A. Trubnikov, Particle interactions in a fully ionized plasma, in: M.A. Leontovich (Ed.), Review in Plasma Physics, vol. 1, Consultants Bureau, New York, 1965, p. 105.
[6] A. Girard, C. Pernot, G. Melin, C. Lécot, Modeling of electron-cyclotron-resonance-heated plasmas, Phys. Rev. E 62 (2000) 1182.
[7] A. Girard, C. Perret, G. Melin, C. Lécot, Modeling of electron-cyclotron-resonance ion source and scaling laws, Rev. Sci. Instrum. 69 (1998) 1100.
[8] J. Killeen, K.D. Marx, The solution of the Fokker–Planck equation for a mirror-confined plasma, in: Meth. Comput. Phys., vol. 9, Alder Academic, New York, 1970, p. 421.
[9] J. Killeen, A.A. Mirin, M.E. Rensink, The solution of the kinetic equations for a multispecies plasma, in: Meth. Comput. Phys., vol. 16, Academic Press, New York, 1976, p. 389.
[10] G.D. Kerbel, M.G. McCoy, Kinetic theory and simulation of multispecies plasmas in tokamaks excited with electromagnetic waves in the ion-cyclotron range of frequencies, Phys. Fluids 28 (1985) 3629.
[11] J. Killeen, G.D. Kerbel, M.G. McCoy, A.A. Mirin, Computational Methods for Kinetic Models of Magnetically Confined Plasmas, Springer, New York, 1986.
[12] C.F.F. Karney, Fokker–Planck and quasilinear codes, Comput. Phys. Rep. 4 (1986) 183.
[13] O. Larroche, Kinetic simulation of a plasma collision experiment, Phys. Fluids B 5 (1993) 2816.
[14] Y.A. Berezin, V.N. Khudick, M.S. Pekker, Conservative finite-difference schemes for the Fokker–Planck equation not violating the law of an increasing entropy, J. Comput. Phys. 69 (1987) 163.
[15] C. Buet, S. Cordier, Conservative and entropy decaying numerical scheme for the isotropic Fokker–Planck–Landau equation, J. Comput. Phys. 145 (1998) 228.
[16] C. Buet, S. Cordier, Numerical analysis of the isotropic Fokker–Planck–Landau equation, J. Comput. Phys. 179 (2002) 43.

[17] C. Buet, S. Cordier, P. Degond, M. Lemou, Fast algorithms for numerical, conservative, and entropy approximations of the Fokker–Planck–Landau equation, J. Comput. Phys. 133 (1997) 310.
[18] L. Chaćon, D.C. Barnes, D.A. Knoll, G.H. Miley, An implicit energy-conservative 2-D Fokker–Planck algorithm, I. Difference scheme, J. Comput. Phys. 157 (2000) 618.
[19] L. Chaćon, D.C. Barnes, D.A. Knoll, G.H. Miley, An implicit energy-conservative 2-D Fokker–Planck algorithm, II. Jacobian-free Newton–Krylov solver, J. Comput. Phys. 157 (2000) 654.
[20] W. Lotz, Electron-impact ionization cross-sections and ionization rate coefficients for atoms and ions from hydrogen to calcium, Z. Phys. 216 (1968) 241.
[21] I.S. Gradshteyn, I.M. Ryzhik, Table of Integrals, Series, and Products, fifth ed., Academic Press, San Diego, 1994.
[22] I. Faille, A control volume method to solve an elliptic equation on a two-dimensional irregular mesh, Comput. Meth. Appl. Mech. Eng. 100 (1992) 275.
[23] H. Niederreiter, Random Number Generation and Quasi-Monte Carlo Methods, SIAM, Philadelphia, 1992.
[24] B.I. Patrushev, A.A. Ivanov, V.P. Gozak, D.A. Frank-Kamenetskii, Low-frequency instability of electron-cyclotron waves in a plasma, Sov. Phys. JETP 32 (1971) 586.
[25] C. Barué, M. Lamoureux, P. Briand, A. Girard, G. Melin, Investigation of hot electrons in electron-cyclotron-resonance ion sources, J. Appl. Phys. 76 (1994) 2662.
[26] A. Girard, P. Briand, G. Gaudard, J.P. Klein, F. Bourg, J. Debernardi, J.M. Mathonnet, G. Melin, Y. Su, The Quadrumafios electron cyclotron resonance ion source: presentation and analysis of the results, Rev. Sci. Instrum. 65 (1994) 1714.
[27] C. Perret, A. Girard, H. Khodja, G. Melin, Limitations to the plasma energy and density in electron cyclotron resonance ion sources, Phys. Plasmas 6 (1999) 3408.
[28] G. Douysset, H. Khodja, A. Girard, J.P. Briand, Highly charged ion densities and ion confinement properties in an electron-cyclotron-resonance ion source, Phys. Rev. E 61 (2000) 3015.
[29] G. Melin, F. Bourg, P. Briand, J. Debernardi, M. Delaunay, R. Geller, B. Jacquot, P. Ludwig, T.K. N'Guyen, L. Pin, M. Pontonnier, J.C. Rocco, F. Zadworny, Some particular aspects of the physics of ECR sources for multicharged ions, Rev. Sci. Instrum. 61 (1990) 236.